

Chapter 5: Black smoker temperatures and the structure of subsurface convection cells

5.1 Introduction

This chapter is concerned with the structure of hydrothermal convection cells in the oceanic crust, associated with mid-ocean ridge spreading centres. The principal aspects of this cell structure – the temperature field and the flow field – are constrained by a variety of physical, chemical and geological observations. The aim of this chapter is to construct the simplest possible convection model which is consistent with these observations. The generally accepted constraints on cell structure, derived from known evidence, are summarised in Figure 5.1

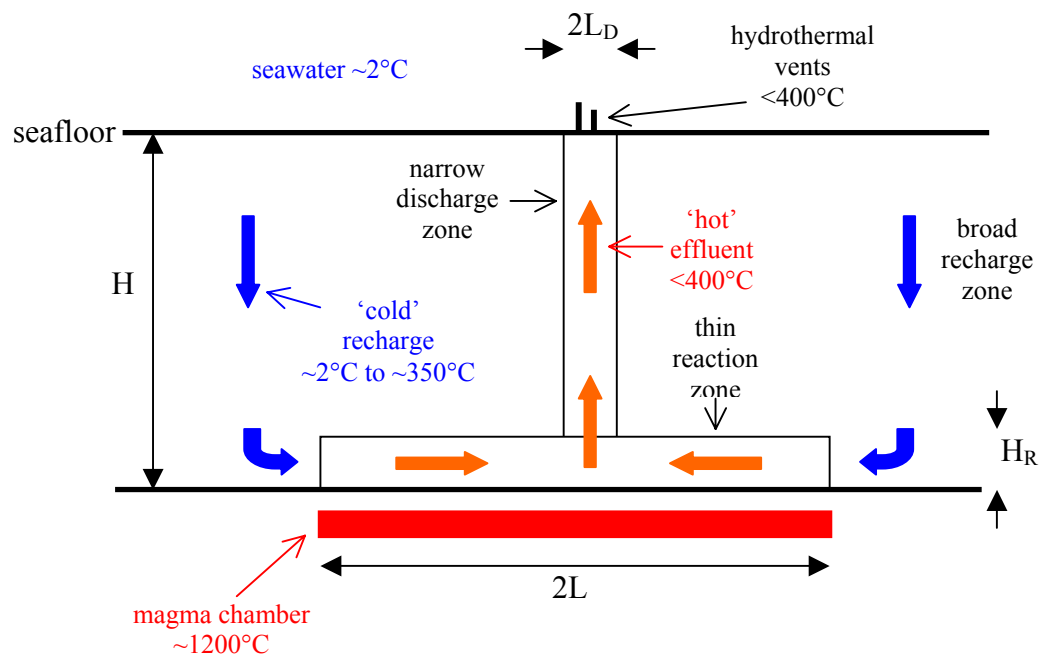


Figure 5.1: Schematic cross-section showing the expected structure of a subsurface hydrothermal convection cell.

The principal features of this prototype seafloor convection cell (Figure 5.1) are discussed below. The energy required to drive the convection of seawater through the crust is supplied by the top surface of the magma chamber (Cann & Strens, 1982; Richardson *et al.*, 1987). It is known that magma solidifies at $\sim 1200^\circ\text{C}$, and so it is assumed that this is the temperature of the heat source driving the convection cell (Lowell *et al.*, 1995). In a typical situation, the

magma chamber is located at a depth $H \sim 1000$ m below the seafloor and has a width $2L \sim 1000$ m (Detrick *et al.*, 1987). Heat from the magma chamber causes seawater to convect through the crust with the general flow pattern indicated in Figure 5.1.

5.1.1 Recharge zone

The downwelling of cold seawater ($\sim 2^\circ\text{C}$) through the crust occurs through a broad recharge zone where temperatures are relatively low ($\ll 350^\circ\text{C}$) (Alt, 1995). As the fluid percolates down through the subseafloor, the temperature begins to rise and the fluid interacts chemically with the surrounding rock, leading to an exchange of chemical elements between the evolved seawater and the crust. The nature of these basalt-seawater reactions is temperature dependent. At 70°C , the reactions are relatively slow - Mg, Na and K are removed from the fluid, whilst Ca and silica are added (Seyfried & Bischoff, 1979). At 150°C , the reactions are more rapid - Mg and sulphate are removed from the water, whilst Ca, Na, K, Fe, Mn, Zn, Cu, Ba and silica are all added (Seyfried & Bischoff, 1979; Seyfried & Mottl, 1982). Finally, above 150°C , Ca and sulphate are removed from the water by anhydrite precipitation (Berndt *et al.*, 1988).

5.1.2 Reaction zone

After the recharge zone, which is characterised by descending fluid flow, the convecting fluid enters a region known as the reaction zone above the top of the solidifying magma chamber. This region is generally thought to occur at the maximum penetration depth of the fluid and is characterised by temperatures in excess of 375°C (Berndt *et al.*, 1989) and horizontal fluid flow. The elevated temperatures in the reaction zone lead to extensive seawater-basalt reactions including the exchange of metals and cations and the further removal of sulphate from the water (Seewald & Seyfried, 1990). Estimates of the typical residence time of fluids in the reaction zone can be made from radioisotope studies and range from less than 3 years (Kadko & Moore, 1988) to 20 years (Grasty *et al.*, 1988). These estimated residence times are compared with the predictions of a numerical convection model in Section 5.4. It is expected that the reaction zone spans a temperature range from $\sim 400^\circ\text{C}$ at its top to $\sim 1200^\circ\text{C}$ at its base. The subsequent vertical temperature gradient gives rise to a conductive heat flux which delivers heat from the magma chamber to the water in the convection cell. Thermal calculations show that the reaction zone must be fairly thin ($H_R \sim 100$ m) in order to maintain the typical power output (~ 100 MW) of a hydrothermal system (Lowell & Germanovich, 1994). These authors argue that such a thin boundary layer might be maintained by downward migration of the hydrothermal system into freshly frozen

magma. It is argued, however, that these mechanisms are not *necessary* in order to restrict the thickness of the thermal boundary layer (Section 5.3). Rather, it is shown that a thin boundary layer spanning the temperature range $\sim 400^{\circ}\text{C}$ to $\sim 1200^{\circ}\text{C}$ is an inevitable consequence of the nonlinear thermodynamic properties of water.

5.1.3 Discharge zone

After the reaction zone, the convecting water enters a discharge zone through which it ascends to the hydrothermal vents on the seafloor. The typical dimensions of a hydrothermally active region of the seafloor (<100 m) are considerably less than the expected dimensions of the magma chamber ($L \sim 1000$ m) and so the upflow zone is often said to be focussed. It is probable that high permeability pathways, due to fractures, faults or textural inhomogeneities in the crust, serve to focus the upflow in the discharge zone. It must be stressed, however, that these inhomogeneities in crustal permeability are not *necessary* in order to impose the required structure on the cell. Some degree of focussing is inevitable in a convection cell, even in the absence of any high permeability pathways (Sections 5.3 & 5.4). Furthermore, by referring to the thermodynamic properties of water it is possible to estimate the half-width of the discharge zone (L_D) as a function of the width of the magma chamber and the crustal permeability (Section 5.4).

Two mechanisms cause the fluid to cool as it rises through the discharge zone - conductive heat loss and adiabatic cooling. The former is caused by horizontal temperature gradients in the discharge zone while the latter is a consequence of depressurisation. As an example, consider a hydrothermal vent field 2.5 km below sea level, where the pressure is ~ 25 MPa. If the reaction zone lies a further 1 km below the seafloor, then the upwelling fluid depressurises from ~ 35 MPa to ~ 25 MPa during its ascent through the discharge zone. Under adiabatic cooling alone, water leaving the reaction zone at $\sim 400^{\circ}\text{C}$ would cool to $\sim 352^{\circ}\text{C}$ on ascent to the seafloor (Haar *et al.*, 1984). The presence of conductive heat loss means that the true degree of cooling in the discharge zone is somewhat greater.

5.1.4 Hydrothermal vents

Finally, after ascending through the discharge zone, the convecting fluid is expelled at hydrothermal vents on the seafloor. The minerals dissolved in the fluid precipitate on contact with the cold ocean waters to form vent chimneys with an internal diameter of ~ 0.01 m to ~ 0.1 m (Lowell *et al.*, 1995). The effluent typically exits from these chimneys at a speed of ~ 1 m.s⁻¹. Thus, if these exit speeds are comparable with the speed of ascent in the discharge

zone, the fluid could ascend from the reaction zone to the seafloor (a distance $H \sim 1000$ m) in a matter of a few minutes (Dickson, 1998). This possibility of a ‘rapid’ ascent is sometimes correlated with the inference that the fluid does not lose much heat on its ascent through the discharge zone (Section 5.2). It might then be argued that a ‘rapid’ ascent is necessary to ensure that conductive heat losses during ascent are minimal. Qualitatively this is true, but it must be stressed that definition of what constitutes a ‘rapid’ ascent depends on the rate at which heat is lost conductively by the ascending fluid. Using a numerical model (Section 5.3), it is shown that minimal heat loss can occur during ascent even when there are no high permeability pathways and the ascent time is as large as several years (Section 5.4).

The most rigid constraint on cell structure is provided by the temperature of the fluid expelled at the seafloor. No hydrothermal effluent hotter than 404°C has ever been observed (Campbell *et al.*, 1988), which is particularly remarkable because it is so much less than the temperature ($\sim 1200^{\circ}\text{C}$) of the heat source (Lister, 1995; Lowell *et al.*, 1995; Wilcock, 1998). Consequently, a successful model for hydrothermal circulation must explain the discrepancy ($\sim 800^{\circ}\text{C}$) between the inferred temperature of the heat source and the observed temperature of the effluent at the seafloor. For some time it has been suspected that the nonlinear thermodynamic properties of water might be responsible for this temperature difference, but the claim has never been rigorously tested or explained (Bischoff & Rosenbauer, 1985; Johnson & Norton, 1991). In Section 5.3, however, the hypothesis is investigated with reference to a full physical model (Jupp & Schultz, 2000). Numerical simulations, and an analysis of the governing equations, are used to show that the thermodynamic properties of water are *sufficient* to impose the $\sim 400^{\circ}\text{C}$ cap on effluent temperatures. This cap applies for any sufficiently hot heat source, and it follows that vent temperatures could remain steady even as the magma chamber solidified and cooled to $\sim 500^{\circ}\text{C}$ (Lowell & Germanovich, 1994).

5.1.5 Summary

In summary, a successful model of hydrothermal convection should have the following features:

- i) A magma heat source of width $L \sim 1000$ m and temperature $\sim 1200^{\circ}\text{C}$ lying at a depth $H \sim 1000$ m below the seafloor. This magma chamber drives convection of seawater in the oceanic crust.
- ii) A seafloor pressure in the range 20 MPa – 40 MPa, corresponding to a depth below sea level of 2 km – 4 km.

- iii) A relatively thin ($H_R \sim 100$ m) thermal boundary layer just above the heat source characterised by a temperature range of $400^\circ\text{C} - 1200^\circ\text{C}$ and predominantly horizontal fluid flow.
- iv) A narrow discharge zone ($2L_D < 100$ m), through which upwelling fluid at $\sim 400^\circ\text{C}$ ascends to the seafloor
- v) Hydrothermal vents on the seafloor, through which fluid emerges at $\sim 350^\circ\text{C}$ to $\sim 400^\circ\text{C}$.

It is argued in Section 5.3 that the properties of water are sufficient to impose a structure on the convection cell which is consistent with all of these constraints. For simplicity, it is assumed that the porosity and permeability of the seafloor are constant and homogeneous. This is a considerable simplification, but it allows the influence of the thermodynamic properties of water to be considered in isolation. Thus, although the real ocean crust is highly inhomogeneous, this inhomogeneity is not *necessary* to explain convection cell structure. The thermodynamic properties of water are *sufficient*, in themselves, to explain this structure.

5.2 Empirical constraints on convection cell structure

Section 5.1 contained a summary of the generally accepted subseafloor structure of a hydrothermal convection cell. This section is dedicated to a review of the observations on which this conceptual model is built. Evidence for the structure of hydrothermal convection cells comes from two types of location – active seafloor systems, and fossil systems exposed in ophiolites. The evidence from these two sources is considered in turn.

The principal evidence from active seafloor systems consists of measurements of the temperature and chemical composition of hydrothermal effluent. Generally, these measurements are obtained using research submersibles which can be piloted to within a few metres of hydrothermal vents. Probes are used to measure the effluent temperature *in situ* and samples of the fluid are collected for later chemical analysis. Thus, the physical and chemical state of the fluid is known as it leaves the discharge zone. Although these data are collected *on* the seafloor, they can be used to constrain the conditions within the convection cell at depth *below* the seafloor.

An example of this process is illustrated in Figure 5.2, using data from a vent 2.5 km below sea level where the seafloor pressure is 25 MPa or 250 bars (Bischoff & Rosenbauer, 1985). The data consist of the measured temperature of the vent (355°C) and the measured concentration of dissolved silica in the vent fluid (1170 ppm). If it is assumed that the fluid has undergone negligible conductive heat loss and negligible chemical reaction on its ascent to the seafloor, the pressure and temperature of the reaction zone from which it ascended can be estimated.

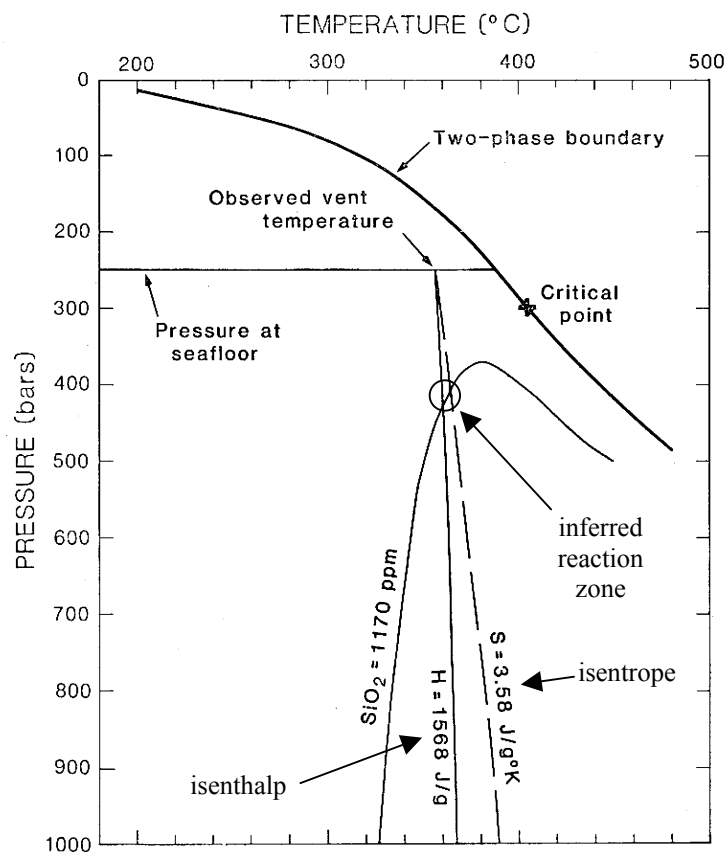


Figure 5.2: An example of the use of geothermometry and geobarometry to infer conditions in the ‘reaction zone’. Diagram from Bischoff & Rosenbauer (1985).

Seawater at 25 MPa and 355°C has a specific enthalpy $h = 1568 \text{ kJ.kg}^{-1}$ and a specific entropy $s = 3.58 \text{ kJ.kg}^{-1}.\text{K}^{-1}$. The corresponding isenthalp and isentrop are plotted in Figure 5.2. If the ascent through the discharge zone were perfectly isenthalpic, the p - T conditions in the reaction zone would lie somewhere on the isenthalp, while if it were perfectly isentropic,

they would lie on the isentrope. The assumption of negligible heat loss means that the ascent lies somewhere between isentropic and isenthalpic. The contour labelled “SiO₂” is the locus of points in the p - T plane for which fluid equilibrated with quartz would have a silica concentration of 1170 ppm. Thus, the assumption of negligible chemical reaction on ascent places the reaction zone somewhere on this contour. Consequently, with the stated assumptions, it can be inferred from Figure 5.2 that the reaction zone occurs at a pressure of ~400 bars (40 MPa) and a temperature of ~360°C. In other words, it must lie ~1.5 km below the seafloor. This example illustrates the use of geothermometry and geobarometry to infer the p - T conditions in the reaction zone. Other studies using the same technique have reached the same general conclusion – that the reaction zone is typically ~1 km below the seafloor and a few tens of degrees hotter than the 350°C - 400°C which is typical of the hydrothermal vents themselves (Von Damm *et al.*, 1985; Campbell *et al.*, 1988).

It should be emphasised that this technique analyses the temperature and composition of vent fluid to estimate the p - T conditions at which the fluid was most recently in physical and chemical equilibrium with the subseafloor. Thus, in terms of the conceptual model of Figure 5.1, it is only the conditions at the boundary of the reaction zone and the discharge zone which can be estimated. Consequently, a typical geothermometry estimate of ~400°C in the reaction zone would not preclude the possibility that the fluid had reached much higher temperatures elsewhere in the reaction zone. It should also be noted that the reaction zone depths inferred by geobarometry (~1 km) are broadly similar to the magma chamber depths inferred by seismic imaging of the seafloor (Detrick *et al.*, 1987). Thus, it seems likely that the reaction zone lies immediately above the magma chamber and spans a temperature range of 400°C to 1200°C (freezing magma) as represented in Figure 5.1.

Palaeo-oceanic crust exposed on land in ophiolite complexes provides the second type of direct evidence for the subseafloor structure of convection cells. In locations such as Cyprus and Oman, fossil hydrothermal systems are exposed in cross-section. It is therefore possible to infer the temperature structure which existed at depth within the fossil system using fluid inclusion geothermometry (Cowan & Cann, 1988) and by analysing the hydrothermal metamorphic mineral assemblages present (Gillis & Roberts, 1999). In particular, Gillis & Roberts (1999) report measurements made at a section of the Troodos Ophiolite in Cyprus. They interpret this section to represent the conductive boundary layer between the hydrothermal convection cell and its magmatic heat source. Their results (Figure 5.3) suggest

that a linear temperature drop from $\sim 1200^{\circ}\text{C}$ to $\sim 400^{\circ}\text{C}$ existed over a vertical distance of ~ 100 m. Thus, this region can be likened to the reaction zone shown in the prototype hydrothermal system of Figure 5.1. Furthermore, their data are consistent with the reaction zone thickness $H_R \sim 100$ m inferred from thermal balance calculations.

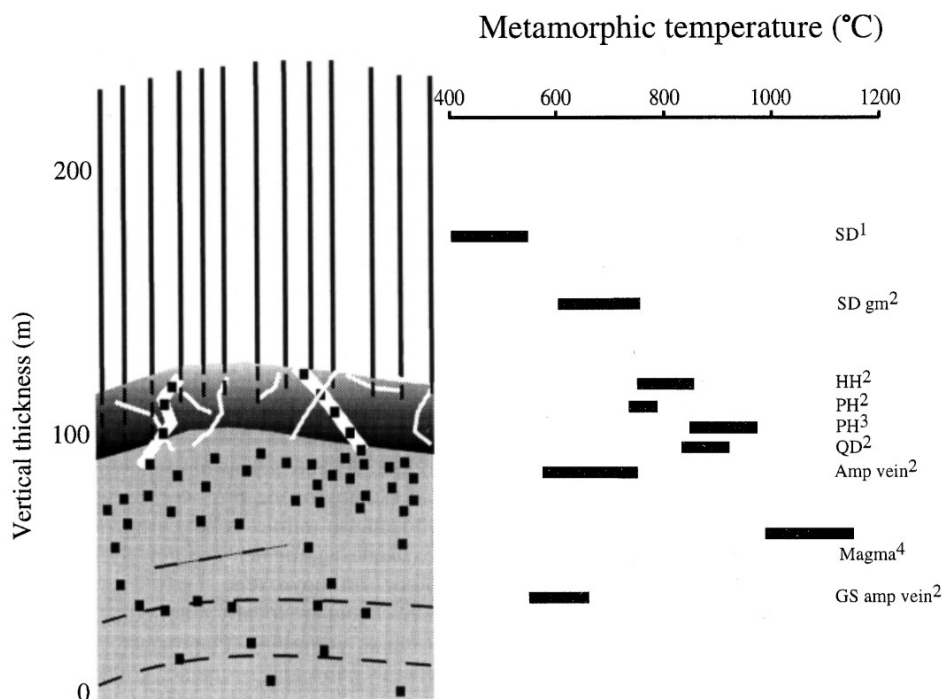


Fig. 3. (Left) Schematic diagram showing typical geological relationships along the sheeted dyke–plutonic transition. Sheeted dykes (vertical lines) are truncated at their base by the gabbroic sequence (light gray). As the contact aureole is approached, the abundance of felsic melt impregnations (solid squares) within the gabbroic sequence increases (up to 30%). The contact aureole is cross-cut by quartz diorite (white lines + solid squares) and amphibole (white lines) veins; these veins show no preferred age relationships. (Right) Thermal conditions in the vicinity of the contact aureole. See text for details. Abbreviations: *SD* = sheeted dykes; *HH* = hornblende hornfels; *PH* = pyroxene hornfels; *QD* = quartz diorite; *GS* = gabbroic sequence; *gm* = groundmass; *1* = mineral assemblage; *2* = plagioclase–amphibole geothermometer; *3* = orthopyroxene–clinopyroxene geothermometer; *4* = lava chemistry.

Figure 5.3: Metamorphic temperatures inferred in an exposed vertical cross section of the Troodos Ophiolite, Cyprus. It is proposed that the contact (dark-shaded) zone between the sheeted dyke complex and gabbroic sequence represents the fossil reaction zone, which once separated the hydrothermal system from its magmatic heat source. Diagram from Gillis & Roberts (1999).

In summary, the evidence pertinent to the structure of hydrothermal convection cells is remarkably consistent, and it is reasonable to place a high degree of confidence in the schematic model of Figure 5.1. However, it is important to understand why a hydrothermal convection cell should adopt this particular structure, and what imposes the $\sim 400^{\circ}\text{C}$ cap on vent temperatures. A working numerical model containing the full thermodynamic properties

of water has been constructed and is used to provide an answer to these questions in the following section.

5.3 A simple model of hydrothermal convection

Three mechanisms have been proposed to impose the $\sim 400^\circ\text{C}$ cap to black smoker temperatures. The first suggestion is that high temperature rock ($>500^\circ\text{C}$) is effectively impermeable, because its ductile nature prevents the formation of cracks (Lister, 1974; Fournier, 1991). The second suggestion is that high temperature rock becomes impermeable over time, either by mineral precipitation infilling fracture porosity (Bischoff & Rosenbauer, 1985; Lowell *et al.*, 1993) or by thermal expansion (Germanovich & Lowell, 1992). Finally, the third suggestion is that the temperature cap is imposed by the thermodynamic properties of water. The first two mechanisms restrict effluent temperature by preventing flow through the hotter, deeper crust. In contrast, the third mechanism allows fluid to flow at *all* temperatures throughout the crust but limits the temperature of the fluid expelled at the seafloor. The purpose of this study is to investigate the third mechanism and the validity of the first two mechanisms is not considered.

Previous studies have shown how the thermodynamic properties of water affect the onset of convection (Straus & Schubert, 1977) and the overall rate of heat transfer in cells operating across a *small* temperature difference ($\sim 10^\circ\text{C}$) (Dunn & Hardee, 1981; Ingebritsen & Hayba, 1994). The advantage of assuming a small temperature difference is that the density can legitimately be regarded as a linear function of temperature. For such systems, it has been shown that cells operating near ~ 22 MPa and $\sim 374^\circ\text{C}$ transfer heat much more rapidly than cells at other temperatures. (The critical point of water, at (~ 22 MPa, $\sim 374^\circ\text{C}$) represents the highest pressure and temperature at which phase separation can occur). Since hydrothermal systems frequently encompass the critical point, this ‘superconvection’ suggests that they might be highly efficient at transferring heat, but it does *not* explain the limit to observed vent temperatures. Real systems operate over a *large* temperature difference ($\sim 10^\circ\text{C}$ to $\sim 1200^\circ\text{C}$) and so the assumption that density depends linearly on temperature is invalid. To explain the narrow range of vent temperatures, no linearising assumptions are made and the focus of the investigation is moved from the overall heat transfer to the internal temperature structure of the cell.

A numerical simulation can be used to illustrate the thermal structure of convection cells (Norton & Knight, 1977). The simulation reported here (Figure 5.4) employs parameter values appropriate to seafloor systems which are outlined below. However, analysis of the governing equations will show that the key features of the cell structure depend solely on the thermodynamics of water, and not on the details of the parametrisation. To isolate the phenomenon under discussion, all previously suggested temperature-limiting mechanisms are excluded, and the crust is taken to be homogeneous and isotropic. Simulations were performed with the package HYDROTHERM (Hayba & Ingebritsen, 1994) (available at <http://water.usgs.gov/software/hydrotherm.html>), which incorporates a look-up table of the thermodynamic properties of pure water. These thermodynamic properties are tabulated only for temperatures above 0°C, and the program terminates when lower temperatures are encountered. If a cold seawater temperature of 2°C is imposed at the seafloor, numerical inaccuracies mean the program occasionally encounters temperatures below 0°C and crashes. To prevent this, a cold seawater temperature of 10°C is imposed. The thermodynamic properties of seawater vary very little between 2°C and 10°C so this approximation has a negligible effect on the solution. The code required a slight modification in order to enforce a particular thermal boundary condition relevant to seafloor systems (Dickson *et al.*, 1995). Hot effluent emerges from an otherwise cold seafloor, so a fixed temperature boundary condition is not always appropriate. Consequently, the condition $\partial T/\partial z = 0$ is imposed on the seafloor where flow is upwards, while $T = 10^\circ\text{C}$ is imposed where flow is downwards.

In Figure 5.4, the top boundary ($z = 1000$ m) represents the permeable seafloor where the pressure is held at 25 MPa (equivalent to ~ 2.5 km below sea surface). The side boundaries for the simulation are at $x = -1700$ m and $x = 1700$ m (beyond the range of Figure 5.4) and are therefore sufficiently distant that they do not influence the solution near the heat source. The side boundaries are held at $T = 10^\circ\text{C}$ and cold hydrostatic pressure throughout the simulation. The bottom boundary ($z = 0$) is impermeable. Parameters for the simulation are porosity = 10%, permeability $k = 10^{-14}$ m², thermal conductivity $\lambda = 2.0$ W.m⁻¹.K⁻¹ (Lowell & Germanovich, 1994).

The governing equations are

- (i) Darcy's law (Faust & Mercer, 1979)
- (ii) An equation of state for pure water (Haar *et al.*, 1984; Watson *et al.*, 1980; Sengers & Kamgar-Parsi, 1984; Sengers & Watson, 1986),

- (iii) The conservation of mass and energy in a porous medium (Faust & Mercer, 1979).

Convection is initiated by a ‘heater’ along part of the bottom boundary (Elder, 1981), which represents the top of the magma chamber. For simplicity, the heater imposes a Gaussian (bell-shaped) temperature profile which runs from ‘cold’ ($T_0 = 10^\circ\text{C}$) at the sides to ‘hot’ ($T_0 + \Delta T$) at the centre. The heater is ‘switched on’ at time zero, when the entire domain is cold ($T = T_0$) and at hydrostatic pressure. Time-dependent solutions for the temperature and pressure fields are calculated and allowed to evolve until a steady state is reached.

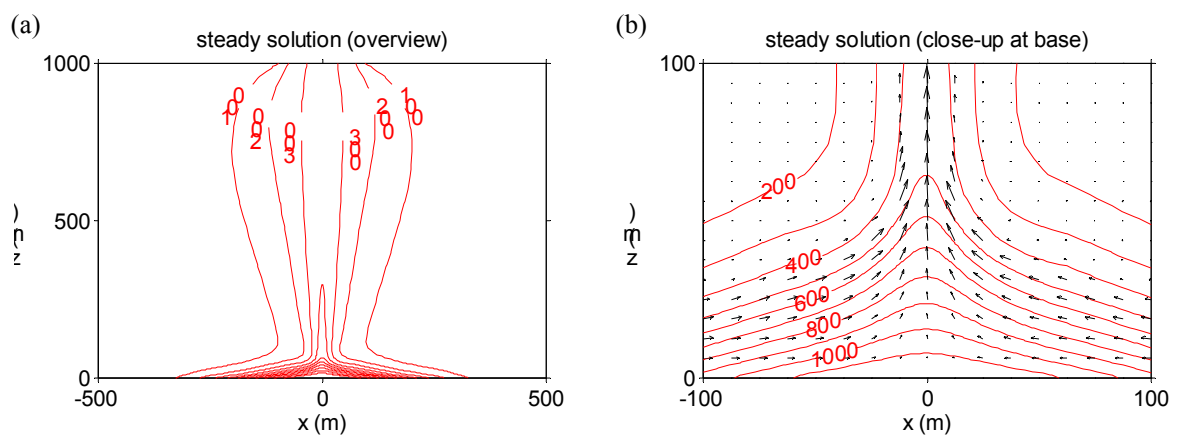


Figure 5.4: The steady state temperature distribution in a convection cell at seafloor pressures, predicted by a HYDROTHERM simulation. (a) The overall temperature structure of the convection cell, showing the distinction between the reaction zone and the discharge zone. Isotherms from 100°C to 1100°C are drawn in red, in increments of 100°C . Flow vectors are omitted for clarity. Flow is downwards at the sides, towards the centre at the base and upwards in the centre. (b) A close-up view of the flow regime and temperature structure inside the boundary layer, showing the bottom 100 m of the domain. Isotherms from 200°C to 1100°C are drawn in increments of 100°C . Vectors are of Darcy velocity.

Figure 5.4 shows a typical steady solution with $T_0 = 10^\circ\text{C}$ and $(T_0 + \Delta T) = 1200^\circ\text{C}$. It is immediately apparent that the main features of the prototype hydrothermal system (Figure 5.1) are reproduced by this simulation. Firstly, there is a thin boundary layer of very hot fluid ($\sim 400^\circ\text{C}$ to 1200°C) at the base of the convection cell, which can be likened to the reaction

zone in Figure 5.1. Secondly, there is an upwelling plume of $\sim 400^\circ\text{C}$ which corresponds to the discharge zone. Similar plume temperatures are obtained for other convectively dominated systems with $T_0=10^\circ\text{C}$ and $(T_0+\Delta T) > \sim 500^\circ\text{C}$, including systems with anisotropic permeability. It follows that vent temperatures could remain steady as a magma chamber solidified and cooled, dropping only when the heat source fell below $\sim 500^\circ\text{C}$ (Lowell & Germanovich, 1994). Numerical experiments suggest that plumes have a natural tendency to form at $\sim 400^\circ\text{C}$, given any sufficient heat source and seafloor pressures. The explanation for this phenomenon lies in the balance between conduction and advection, the two mechanisms which transport energy, as the system evolves.

In the model (Figure 5.4), the temperature (T) and pressure (p) are functions of position ($\mathbf{x}=(x,z)$). Thermal gradients produce a conductive heat flux $-\lambda\nabla T$, where λ is the thermal conductivity. Fluid motion creates an advective heat flux $\rho h\mathbf{u}$, for water of density ρ , specific enthalpy h and Darcy velocity \mathbf{u} . In the conservation of energy equation (Faust & Mercer, 1979) the rate of change of energy per unit volume is given by the negative divergence of the total heat flux, $-\nabla\cdot(\rho h\mathbf{u}-\lambda\nabla T)$. This can be split into two terms, $-\nabla\cdot(\rho h\mathbf{u})$ and $\lambda\nabla^2 T$, which are the rates of accumulation of energy per unit volume, due to the advection and conduction of heat respectively. At any point in the cell, the relative importance of these two mechanisms can be expressed by the ratio:

$$Ra_L(\mathbf{x},t) = \left| \frac{\nabla\cdot(\rho h\mathbf{u})}{\lambda\nabla^2 T} \right| \quad (5.1)$$

This ratio, which is a function of time and space, measures the influence of fluid motion on the evolution of the local temperature field, and could logically be labelled the ‘local Rayleigh number’. (Traditionally, a single fixed parameter - the Rayleigh number - is defined for the whole cell (Straus & Schubert, 1977). Here a ‘local Rayleigh number’ has been assigned independently to each point in the cell, and is allowed to change with time.) Conduction dominates over advection at any point where $Ra_L \ll 1$ and the temperature evolves independently of any fluid flow. Conversely, where advective heat transfer is strong enough to influence the evolution of the temperature field, $Ra_L \gg 1$ and the isotherms are distorted away from a conductively dominated pattern. Advective distortion of the isotherms marks the separation of the plume from the boundary layer and effectively *defines* the plume in Figure 5.4. To understand where and when plumes initiate as the simulation progresses, it is important to know where and when the local Rayleigh number is maximised.

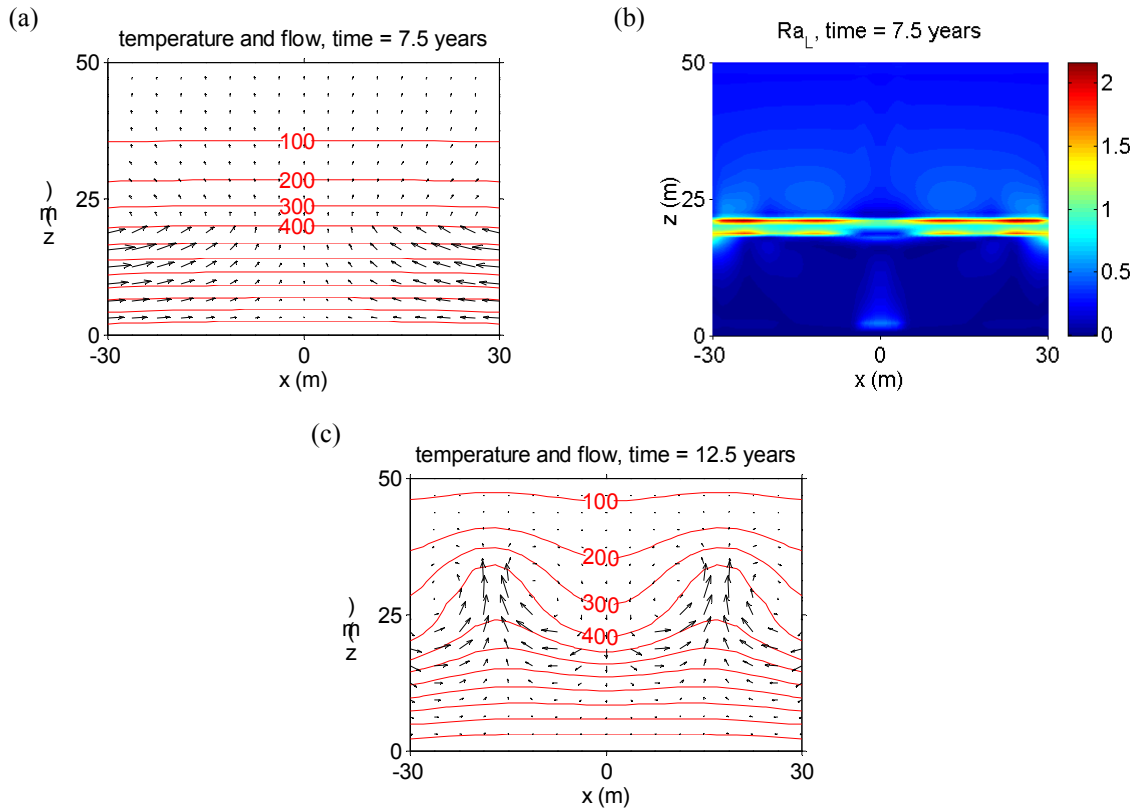


Figure 5.5: The bottom of the domain shown in Figure 5.4, shown at the early stages of the simulation, before a steady state has been reached. (a) The temperature and flow fields just before plume formation. The thermal structure is governed by conduction alone. Convective motion exists, but it does not influence the temperature field. (b) Colour plot of the local Rayleigh number Ra_L , just before plume formation. The regions of greatest Ra_L indicate where plumes are likely to form. (c) The temperature and flow fields just after plume formation. Advection has begun to distort the thermal structure. (As the simulation progresses to steady state, these two plumes coalesce to form the single plume in Figure 5.4). Isotherms are drawn in red from 100°C (top) to 1100°C (bottom) in increments of 100°C. Vectors are of Darcy velocity.

After the heater is switched on, a thermal signal propagates upwards (Figure 5.5). For the period before plume formation (Figures 5.5a,b), the approximate magnitudes of the energy accumulation terms can be calculated. Let d be the distance that the signal has penetrated into the domain, i.e. the vertical range over which the temperature drops from ‘hot’ ($T_0 + \Delta T$) to ‘cold’ (T_0). Denote by Φ the order of magnitude of the advective heat flux $|\rho h \mathbf{u}|$. Then,

$|\nabla \cdot (\rho h \mathbf{u})|$ is of order Φ/d , and $|\lambda \nabla^2 T|$ is of order $\lambda(\Delta T)/d^2$. Consequently, the local Rayleigh number (Ra_L) is of order $(\Phi/\lambda(\Delta T)) \cdot d$, and therefore scales linearly with the vertical length scale d . Just before plume formation, d is sufficiently small that Ra_L is everywhere of order unity (Figure 5.5b). It is important to note, however, that Ra_L is greatest near the 400°C isotherm. A short time later, when d , and hence Ra_L , have increased slightly, plumes have started to form at about 400°C (Figure 5.5c).

By making some simplifications, it is possible to explain why Ra_L is maximised at ~400°C just before plume formation. At this early stage, when the temperature field is governed by conduction alone, temperature gradients are nearly uniform (Figure 5.5a). It therefore follows, from equation (5.1), that the maximum value of Ra_L is controlled by the maximum value of $|\nabla \cdot (\rho h \mathbf{u})|$. Above the level of horizontal flow, there can be no significant horizontal pressure gradient. It follows that the vertical pressure gradient must be approximately equal in the cold recharge zone, where fluid descends, and the hot discharge zone, where fluid ascends (Pascoe & Cann, 1995). This vertical pressure gradient must be sufficiently small for cold water to descend in the recharge zone, and sufficiently large for hot water to ascend in the discharge zone. Hence, the vertical pressure gradient must lie between hot hydrostatic and cold hydrostatic. The permeability is the same in both limbs, but the total resistance to flow is much greater in the upflow limb because of its smaller cross-sectional area (Figures 5.1, 5.4a). It follows that the vertical pressure gradient is much closer to cold hydrostatic than hot hydrostatic.

Hence, above the level of horizontal flow:

$$\frac{\partial p}{\partial z} \approx -g\rho_0 \quad (5.2)$$

where ρ_0 is the density of cold water. Suppose that the advective heat flux $\rho h \mathbf{u}$ is dominated by its vertical component which, by Darcy's law, is

$$\rho h w = -k \left(\frac{\partial p}{\partial z} + g\rho \right) \frac{\rho h}{\mu} \quad (5.3)$$

for permeability k , gravitational acceleration g , and dynamic viscosity μ . From equations (5.2) and (5.3), an approximate expression for the advective energy accumulation is then

$$-\nabla \cdot (\rho h \mathbf{u}) \approx \left[\frac{\partial}{\partial z} \left(\frac{(\rho_0 - \rho)\rho h}{\mu} \right) \right] \cdot [-gk] = -gk \left[\frac{\partial F}{\partial z} \right] \quad (5.4)$$

where the 'fluxibility' of the fluid (F) is defined (Lister, 1995) to be

$$F = \frac{(\rho_0 - \rho)\rho h}{\mu} \quad (5.5)$$

It follows from equations (5.1) and (5.4) that Ra_L should be maximised, and plumes will form, where $|\partial F/\partial z|$ is maximised.

The ‘fluxibility’ (F) is a function of the thermodynamic state of the fluid (Figures 5.6k,l) and is a scaled version of the vertical advective heat flux in a cold hydrostatic pressure gradient. (The true vertical advective heat flux, in $\text{W}\cdot\text{m}^{-2}$, is given by the product gkF). Since plumes are expected to form where spatial gradients in fluxibility are greatest, it is important to consider, in detail, the dependence of the fluxibility on pressure and temperature. Figure 5.6 summarises the temperature- and pressure-dependence of the fluxibility and the thermodynamic properties on which it depends. The density of cold water (ρ_0) is a constant and ρ , μ and h are given as functions of pressure and temperature by the steam tables embedded in the HYDROTHERM code (Haar *et al.*, 1984; Watson *et al.*, 1980; Sengers & Kamgar-Parsi, 1984; Sengers & Watson, 1986).

Figures 5.6a,b reveal the variation in fluid density (ρ) over a range of pressures and temperatures relevant to seafloor hydrothermal systems. It is clear that the density varies greatly with temperature and little with pressure, producing a marked density drop at $\sim 400^\circ\text{C}$ to $\sim 500^\circ\text{C}$ for all seafloor pressures. Below the critical pressure of 22 MPa ($\sim 2.2\text{km}$ hydrostatic head), this density drop is discontinuous, and is caused by a change of state from liquid to vapour as the water boils. However, above 22 MPa pure water has no boiling point and cannot coexist as two separate phases. Consequently, the density is a continuous function of temperature. There is still a fairly sharp drop in density at $\sim 400^\circ\text{C}$ (Figure 5.6b), but it is not caused by boiling because there is no discontinuity and no phase change. Therefore, for all seafloor pressures above 22 MPa, the water shows a smooth transition from a ‘liquid-like’ state below $\sim 400^\circ\text{C}$ to a ‘gas-like’ state above $\sim 400^\circ\text{C}$.

Figures 5.6c,d reveal the variation in specific enthalpy (h) over the same section of p - T space. The specific enthalpy is a measure of the energy content of the fluid per unit mass and is always quoted relative to some reference state. The reference state for these data, for which h is assigned the value zero, is $p = 0.1\text{ MPa}$, $T = 0^\circ\text{C}$. However, it is clear from the figures that $h \approx 0$ when $T \approx 0^\circ\text{C}$ for all relevant seafloor pressures. Therefore, it can be

assumed with minimal error that all ‘cold’ fluid in a hydrothermal convection cell has zero specific enthalpy.

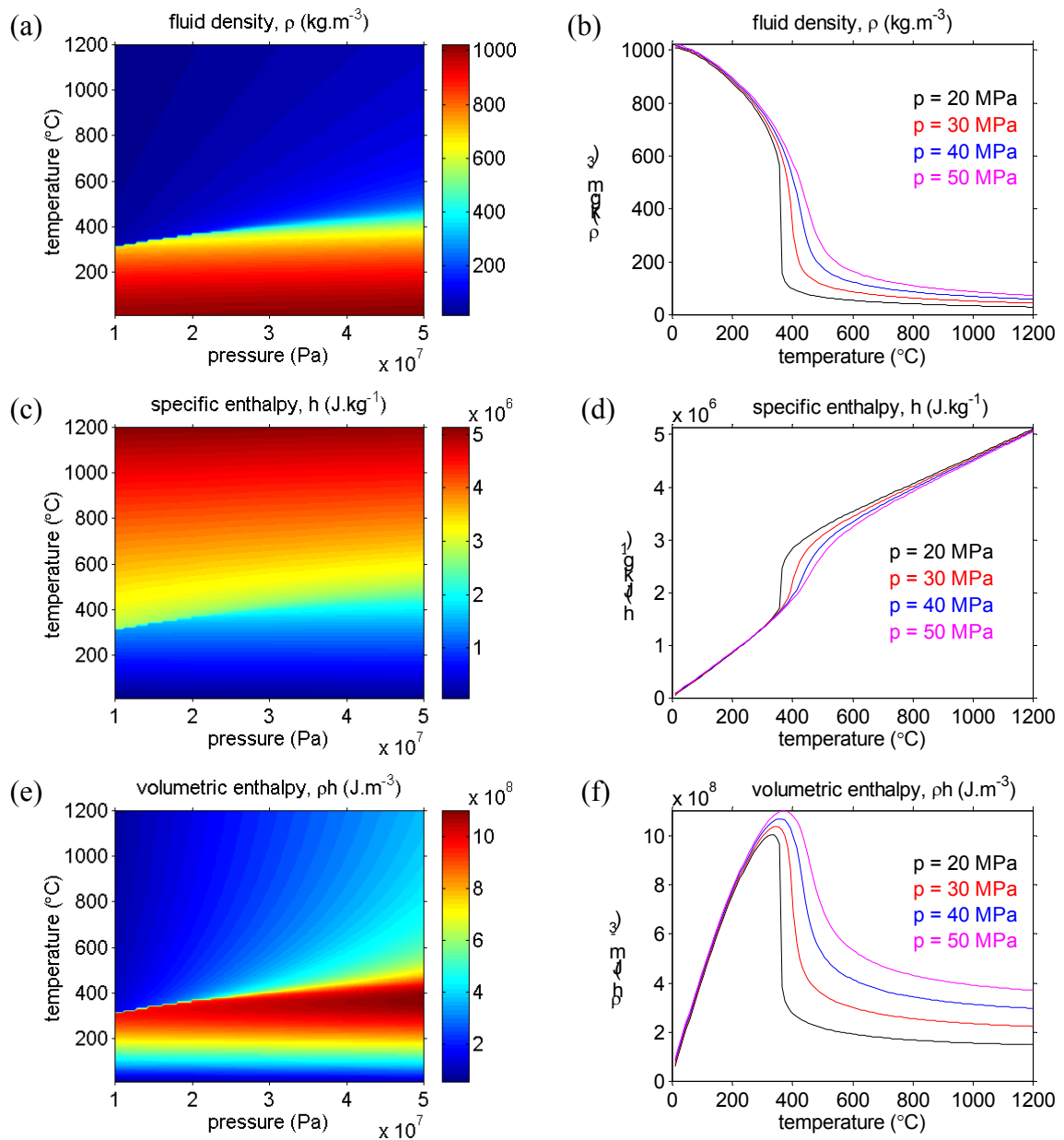


Figure 5.6: The dependence of the thermodynamic properties of pure water on pressure and temperature. Values are taken from the tables embedded in the HYDROTHERM code. The pressure range of 10 MPa to 50 MPa corresponds to depths of between 1km and 5km below sea level. (a) & (b) The density (ρ). (c) & (d) The specific enthalpy (h). (e) & (f) The volumetric enthalpy (ρh).

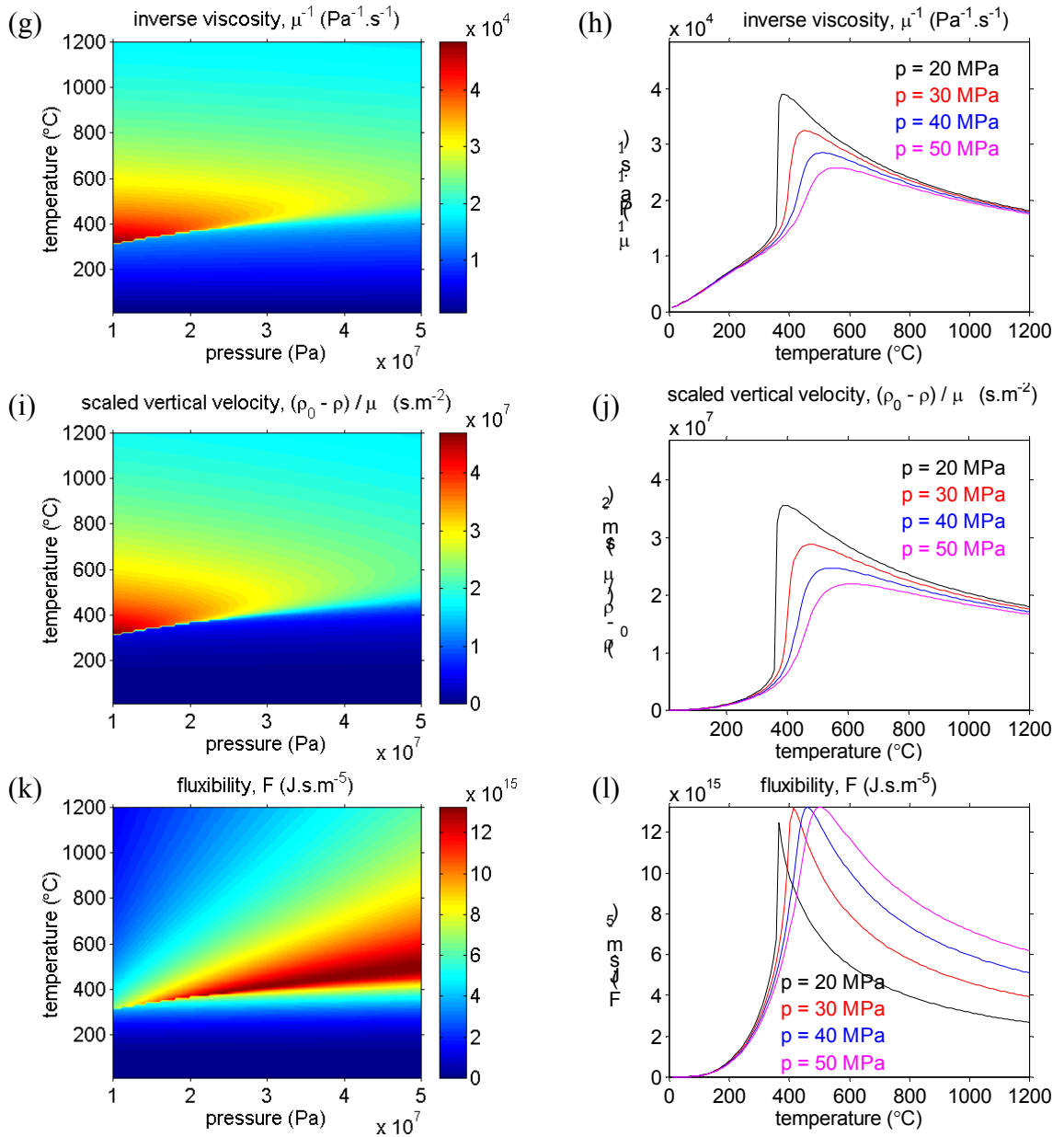


Figure 5.6: (continued) The dependence of thermodynamic variables on the pressure and temperature of the fluid. Values are for pure water and are taken from the tables embedded in the HYDROTHERM code. The pressure range of 10 MPa to 50 MPa corresponds to depths of between 1km and 5km below sea level. (g) & (h) The inverse viscosity (μ^{-1}). (i) & (j) The scaled vertical velocity ($(\rho_0 - \rho) / \mu$) of fluid in a cold hydrostatic pressure gradient $g\rho_0$. The true vertical velocity (in m·s⁻¹) is $[gk] \cdot [(\rho_0 - \rho) / \mu]$. (k) & (l) The fluxibility ($F = (\rho_0 - \rho)\rho h / \mu$). In a cold hydrostatic pressure gradient, the buoyancy-driven energy flux (in W·m⁻²) is $[gk] \cdot F$.

Figure 5.6d shows that the specific enthalpy is a monotonic increasing function of temperature for all pressures. It is common in the literature to find references to the specific heat capacity (c_p) of hydrothermal fluid but it is suggested that reference to it is unnecessary and potentially misleading. At a given pressure, the specific heat capacity is defined by the relation $c_p(p,T) = \partial h/\partial T$, and so represents the slope of the lines in Figure 5.6d. For sub-critical pressures (<22 MPa) the phase change associated with boiling causes a discontinuity in the graph of enthalpy (h) against temperature (T). The magnitude of this discontinuity is equal to the latent heat of vaporisation at that pressure, and it is sometimes argued that its existence causes the value of the specific heat capacity to approach infinity as the discontinuity is approached. This is highly misleading as it can lead to the erroneous argument that an infinite amount of energy is required to heat the fluid beyond its boiling point. However, the discontinuity simply means that the specific heat capacity is *undefined* at the boiling point. For this reason, and since the specific enthalpy is a more fundamental quantity (from which the specific heat capacity is derived), no further attention is paid to specific heat capacities in this chapter.

The volumetric enthalpy (ρh) is a measure of the energy content of the fluid *per unit volume* (Figures 5.6e,f). Unlike the specific enthalpy (h) it is not a monotonic increasing function of temperature; on the contrary, for seafloor pressures it is maximised at $\sim 400^\circ\text{C}$ (Figure 5.6f). In other words, at seafloor pressures, 1 m^3 of water at $\sim 400^\circ\text{C}$ contains more energy than 1 m^3 of water at *any other temperature*.

Figures 5.6g,h show the dependence of the inverse fluid viscosity (μ^{-1}) on pressure and temperature. (The figure shows inverse viscosity (μ^{-1}) rather than viscosity (μ) because the resulting graph is clearer.) Figure 5.6h shows that the viscosity is least (equivalently, the inverse viscosity is greatest) at $\sim 400^\circ\text{C}$. In other words, at seafloor pressures water ‘flows more readily’ at $\sim 400^\circ\text{C}$ than at *any other temperature*.

Figures 5.6i,j show how the quantity $(\rho_0 - \rho)/\mu$ depends on pressure and temperature. This quantity is named the ‘scaled vertical velocity’ because in a cold hydrostatic pressure gradient ($g\rho_0$) the vertical velocity of upwelling fluid is $w = gk(\rho_0 - \rho)/\mu$. Figure 5.6j shows that the scaled vertical velocity is maximised at $\sim 400^\circ\text{C}$ for seafloor pressures. In other words, in a regime of cold hydrostatic pressure water ascends more quickly at $\sim 400^\circ\text{C}$ than at *any other temperature*. This effect is due to a viscosity minimum for water at $\sim 400^\circ\text{C}$

(Figure 5.6j). Hotter fluid is always less dense than colder fluid and so has greater buoyancy (Figure 5.6a,b). As temperatures rise above $\sim 400^\circ\text{C}$, however, the viscosity (μ) which resists the flow increases faster than the density drop ($\rho_0 - \rho$) which drives the flow. Above $\sim 400^\circ\text{C}$, therefore, hotter fluid would actually ascend more slowly than colder fluid.

Finally, Figures 5.6k,l reveal the dependency of the fluxibility (F) on pressure and temperature. The fluxibility is the product of the scaled vertical velocity (Figures 5.6i,j) and the volumetric enthalpy (Figures 5.6e,f). At $\sim 400^\circ\text{C}$ upwelling water displays its maximum vertical velocity (Figure 5.6j) and carries a maximum quantity of thermal energy per unit volume (Figure 5.6f). In summary for seafloor pressures, the fluxibility (F) - and hence the vertical advective heat flux (gkF) - is maximised between $\sim 400^\circ\text{C}$ and $\sim 500^\circ\text{C}$.

Now that the pressure- and temperature-dependence of fluxibility (F) has been established it is appropriate to return to the subject of plume formation. It is deduced, following equation (5.5), that upwelling plumes are expected to form where $|\partial F/\partial z|$ is maximised. It is clear from Figure 5.6k that in a seafloor hydrothermal system the fluxibility varies greatly with temperature, but little with pressure. Before the formation of a plume, temperature is approximately a linear function of height (Figure 5.5a). Thus, $|\partial F/\partial z|$ should be maximised approximately where $|\partial F/\partial T|$ is maximised.

Figure 5.7a shows $|\partial F/\partial T|$ as a function of temperature for a range of seafloor pressures. The approximate plume formation temperature ($T_p(p)$) can be defined as the temperature for which $|\partial F/\partial T|$ is maximised for a given pressure (p). Figure 5.7b shows that $T_p \approx 410^\circ\text{C}$ for $p=35$ MPa which is the approximate pressure at the base of the convection cell in Figures 5.4 and 5.5. Thus, 410°C is the temperature at which plumes would separate from the boundary layer, under the simplifying assumptions. The fact that this predicted plume formation temperature is consistent with the numerical simulation (Figure 5.5c) provides *a posteriori* evidence that the various simplifying assumptions (cold hydrostatic pressure gradient, advective flux dominated by vertical component) are justified.

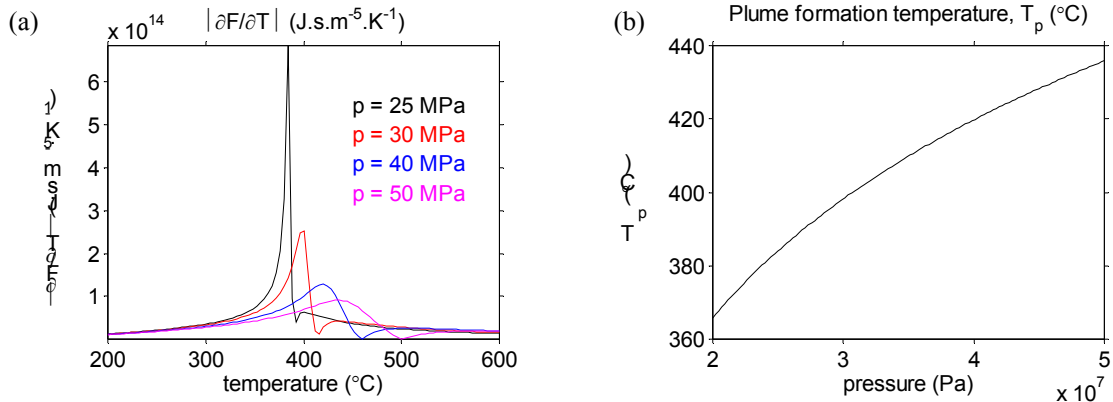


Figure 5.7: The estimated plume formation temperature (T_p) for pure water at seafloor pressures. At a given pressure (p) the plume formation temperature (T_p) is the temperature at which $|\partial F/\partial T|$ is maximised. (a) $|\partial F/\partial T|$ as a function of temperature for a range of seafloor pressures. (b) T_p as a function of pressure.

A highly significant simplification in this analysis has been the assumption that the convecting fluid is pure water rather than salt water. Although the thermodynamic properties of water at *constant* salinity have been known for some time (Bischoff & Rosenbauer, 1985; Anderko & Pitzer, 1993), they are insufficient for use in numerical simulations. If salt is to be included in the calculations, an equation for the conservation of salt must be added to the equations for conservation of mass, energy, and momentum which govern the pure water system. This is a considerable complication. Furthermore, unlike pure water, salt water can boil at *all* seafloor pressures. Therefore it would be necessary to track the progress of two evolving fluids, with varying salinities, at temperatures above $\sim 400^\circ\text{C}$. The thermodynamic properties of salt water as functions of the *three* independent variables pressure, temperature and salinity have only recently been published (Palliser & McKibbin, 1998a, 1998b, 1998c). Consequently, numerical codes to explore the nature of salt-water convection in the seafloor are in their infancy and have yet to produce conclusive results (Wenyue Xu, *pers. comm.*, 1999). The question of salt water convection is discussed further in Chapter 7, but it is sufficient to note for now that the fluxibility of salt water could, in principle, be defined in exactly the same fashion as for pure water (equation (5.5)). A complication arises, however, because the fluxibility will depend on salinity. Salinity is well constrained in the ocean, but may be considerably different at depth within the seafloor because of phase separation and chemical interaction with the rock. Thus, the results of numerical experiments incorporating the full thermodynamic properties of salt water must be awaited for the issue to be resolved.

As an example, however, the thermodynamic properties of a 3.2% NaCl solution (Bischoff & Rosenbauer, 1985) suggest that T_p would be shifted upwards by $\sim 30^\circ\text{C}$ compared with the results for pure water.

Although it is a considerable simplification, the use of pure water has the following definite advantage. At pressures greater than 22 MPa (seafloor depth ~ 2.2 km), pure water is a single-phase fluid. Therefore, the complication of phase separation can be removed from this analysis and it has been possible to demonstrate a temperature-limiting mechanism which is independent of ‘phase-separation’ or ‘two-phase effects’. This suggests that, although phase separation undoubtedly occurs in active hydrothermal systems, it is not *necessary* in order to explain convection cell structure.

Three differences between this approach and classical studies of porous medium convection (Lapwood, 1948) should be noted. Firstly, in this study convection is not generated by a *uniformly* heated lower boundary. The presence of both hot and cold regions at the base of the cell ensures that there is always a horizontal temperature gradient and associated fluid flow. Consequently, the point of interest is not the onset of convective motion, but the onset of convective distortion of the temperature field. Secondly, no use is made of the Boussinesq approximation (Phillips, 1991) under which the advective heat flux would be approximated by $\rho_0 h \mathbf{u}$. The Boussinesq approximation is valid for cells with *small* temperature differences, where $\rho \approx \rho_0$, but in this study the true advective heat flux ($\rho h \mathbf{u}$) is used because ρ can vary from ρ_0 by a factor of 25 (Figures 5.6a,b). Thirdly, this analysis abandons the traditional Rayleigh number, which is an *overall* balance between advection and conduction, in favour of a *local* Rayleigh number which gives the balance at each point in the cell as a function of time. This permits identification of the precise position and temperature at which plumes form.

At a given pressure, and given a sufficient heat source, a plume will form at temperature T_p , the temperature at which $|\partial F/\partial T|$ is maximised (Figure 5.7). If ambient pressures are known plume formation temperatures can be inferred for single-phase hydrothermal systems. Observed vent temperatures may be cooler than this plume formation temperature because of conductive losses from the ascending fluid, but they cannot be hotter.

5.4 Scaling Analysis

It has been shown that the thermodynamic properties of water can exert a strong influence on the structure of a seafloor convection cell. In the previous section it is supposed, for simplicity, that the permeability of the host rock is constant and homogeneous. Consequently, the observed convection cell structure (Figure 5.4) is governed by the thermodynamic properties of water. Despite the deliberate simplicity of the model, the simulated convection cell displays all three key features required by the existing evidence (Figure 5.1): (i) a thin ‘reaction zone’, (ii) a narrow ‘discharge zone’ and (iii) seafloor vents which are limited to $\sim 400^\circ\text{C}$. This section is concerned with the length- and time-scales associated with the reaction zone and the discharge zone. Phillips (1991) shows how the approximate dimensions of the plume and the basal thermal boundary layer can be calculated for a convection cell in a porous medium. Given that the driving temperature difference is *small*, Phillips assumes that the viscosity (μ) is constant and that the enthalpy (h) and density (ρ) are linear functions of temperature. Phillips also invokes the Boussinesq approximation. The following argument follows that of Phillips (1991), with the difference that the full, nonlinear thermodynamic properties of water are retained.

5.4.1 Cartesian geometry

Suppose that the seafloor convection cell is driven by a magma chamber of half-width L which lies at a depth H below the seafloor, as in Figure 5.1. It has been shown in Section 5.3 that the 400°C isotherm marks the approximate boundary of two important regions of the convection cell – the reaction zone and the discharge zone. The thickness of the reaction zone is denoted by H_R , and the half-width of the discharge zone is denoted by L_D . For the moment, it is assumed that Figure 5.1 represents convection in two spatial dimensions, so that the magma chamber extends indefinitely in the third dimension along the ridge-axis.

There is little horizontal flow above the reaction zone and therefore horizontal pressure gradients are negligible. However, below this level there is considerable horizontal flow from the recharge zone into the reaction zone. Within the reaction zone itself, the flow of hot fluid (of density ρ and viscosity μ) is predominantly horizontal, and so the vertical pressure gradient must be approximately equal to the hot hydrostatic value, $g\rho$. Outside the reaction zone, at the base of the cell, the flow of cold water (of density ρ_0) is also predominantly horizontal. In this region, therefore, the vertical pressure gradient must be approximately

equal to the cold hydrostatic value, $g\rho_0$. At the base of the cell, the difference between the hot and cold hydrostatic pressure regimes - inside and outside the reaction zone - applies over a vertical distance of H_R . Thus, it follows that the horizontal pressure difference driving fluid into the reaction zone is given, approximately, by

$$\Delta p \sim (\rho_0 - \rho)gH_R \quad (5.6)$$

This pressure difference operates over a horizontal distance L , and so by Darcy's law the horizontal velocity of fluid flowing in the reaction zone is

$$u \sim \frac{k}{\mu} \frac{\Delta p}{L} = gk \frac{(\rho_0 - \rho)}{\mu} \frac{H_R}{L} \quad (5.7)$$

The vertical velocity of fluid in the discharge zone is given by

$$w \sim gk \frac{(\rho_0 - \rho)}{\mu} \quad (5.8)$$

Hence, conservation of mass in the reaction zone implies that

$$2\rho uH_R \sim 2\rho wL_D \quad (5.9)$$

Equations (5.7), (5.8) and (5.9) can then be combined to express the mass balance as

$$H_R^2 \sim L_D L \quad (5.10)$$

The energy balance of the reaction zone is a balance between conduction and advection. If the vertical temperature drop across the reaction zone is ΔT , the system is driven by a vertical conductive heat flux of approximate magnitude $\lambda(\Delta T) / H_R$. This heat flux operates over a horizontal distance $2L$ and is balanced by the advective transport of heat into the upflow zone. This advective heat transport consists of 'hot' fluid of specific enthalpy h flowing at a speed w over a horizontal distance $2L_D$. Consequently, the conservation of energy in the reaction zone is expressed by the balance

$$2L \frac{\lambda \Delta T}{H_R} \sim 2\rho h w L_D \quad (5.11)$$

Using the definition of the fluxibility (F) (equation (5.5)) this can be re-arranged to give:

$$\frac{L \lambda (\Delta T)}{L_D H_R} \sim gk \left(\frac{\rho h (\rho_0 - \rho)}{\mu} \right) = gkF \quad (5.12)$$

Equations (5.10) and (5.12) can now be solved to give the approximate magnitudes of the two unknown lengthscales L_D and H_R :

$$L_D \sim \left[\frac{\lambda (\Delta T)}{gF} \right]^{2/3} L^{1/3} k^{-2/3} \quad (5.13)$$

$$H_R \sim \left[\frac{\lambda(\Delta T)}{gF} \right]^{1/3} L^{2/3} k^{-1/3} \quad (5.14)$$

The greatest uncertainty in these expressions resides in the value of the permeability (k) which is very poorly constrained. Plausible values for the permeability of the seafloor range over several orders of magnitude, from 10^{-17} m^2 to 10^{-11} m^2 (Table 6.1), and it is possible that the presence of fractures and fault conduits could make the effective bulk permeability even greater. In contrast, the other parameters on which these scalings depend are relatively accurately known. The gravitational acceleration (g) is constant ($g = 9.8 \text{ m.s}^{-2}$), while the thermal conductivity for a water/rock mixture can be estimated with confidence ($\lambda = 2 \text{ W.m}^{-1}.\text{K}^{-1}$). The solidifying magma chamber is taken to be at 1200°C and the boundaries of the upflow and reaction zones are clearly marked by the temperature at which pure water changes from a liquid-like state to a gas-like state. This transition occurs at $\sim 400^\circ\text{C}$ for all relevant seafloor pressures and therefore the temperature drop across the reaction zone is also well constrained ($\Delta T = 800 \text{ K}$). Finally, the fluxibility of hot, upwelling water changes little over the relevant temperature range (Figures 5.6k,l) and a value of $F = 1.2 \cdot 10^{16} \text{ J.s.m}^{-5}$ is typical for all seafloor pressures. Thus, the quantity in square brackets in equations (5.13) and (5.14) takes approximately the same value for all seafloor hydrothermal systems:

$$\left[\frac{\lambda(\Delta T)}{gF} \right] \approx 1.36 \cdot 10^{-14} \text{ m}^3 \quad (5.15)$$

It is likely that the half-width of the magma chamber (L) will vary from location to location, but a value of 500 m (i.e. a magma chamber 1 km wide) is probably typical. Taking $L = 500 \text{ m}$ implies that, in SI units:

$$L_D \sim 4.52 \cdot 10^{-9} \cdot k^{-2/3} \quad (5.16)$$

$$H_R \sim 1.45 \cdot 10^{-3} \cdot k^{-1/3} \quad (5.17)$$

It must be remembered that these are only order of magnitude estimates, because they are derived from approximate balances rather than strict equalities. The values predicted by equations (5.16) and (5.17) can be compared with the results of the numerical simulation of Section 5.3, for which $k = 10^{-14} \text{ m}^2$ and $L \approx 500 \text{ m}$. With these values, equations (5.16) and (5.17) predict that $L_D \approx 10 \text{ m}$ and $H_R \approx 67 \text{ m}$. Comparison with Figure 5.4 shows that the estimate for H_R is about a factor of 2 too small, while the estimate for L_D is about a factor of 10 too small. Consequently, equations (5.16) and (5.17) can be made more accurate by the introduction of dimensionless factors. The lengthscales, in SI units, then become:

$$L_D \approx 4.52 \cdot 10^{-8} \cdot k^{-2/3} \quad (5.18)$$

$$H_R \approx 2.90 \cdot 10^{-3} \cdot k^{-1/3} \quad (5.19)$$

The graphs in Figure 5.8a show how these lengthscales depend on the permeability (k) according to equations (5.18) and (5.19).

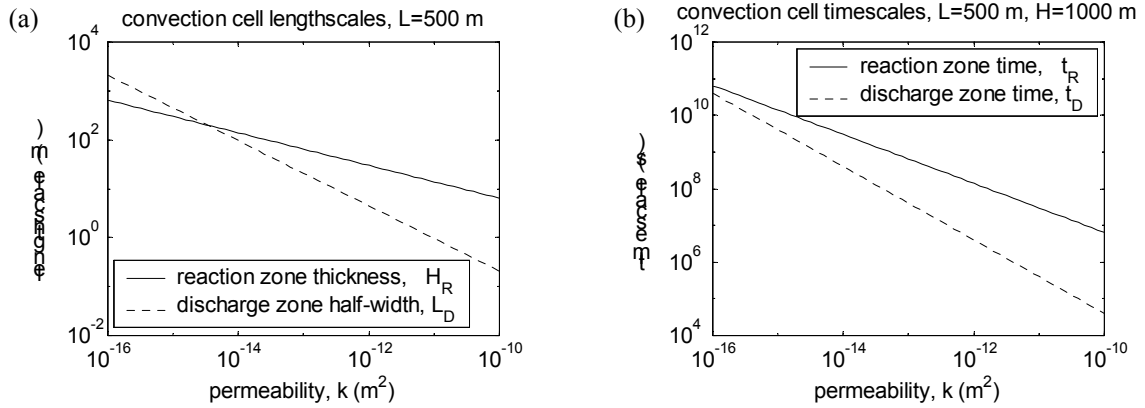


Figure 5.8: The length- and time-scales associated with the reaction and discharge zones in 2-d Cartesian geometry, for a magma chamber of width $2L = 1000$ m. (a) Lengthscales from equations (5.18) and (5.19). (b) Timescales from equations (5.21) and (5.23).

If it is assumed that the seafloor is homogeneous, these equations could be used to constrain seafloor permeability given a knowledge of the magma chamber width ($2L$). In an active seafloor system seismic imaging may provide this information, whilst in an ophiolite it may be possible to deduce this from direct observation. If either the reaction zone thickness (H_R) or the discharge zone half-width (L_D) could be estimated, an estimate for the bulk permeability could be made.

5.4.2 Residence times in the discharge and reaction zones

The approximate magnitude of the time taken for fluid to ascend the discharge zone is:

$$t_D \sim \frac{H}{w} = \left[\frac{H}{g} \left(\frac{\mu}{\rho_0 - \rho} \right) \right] \cdot k^{-1} \quad (5.20)$$

With $H = 1000$ m, $(\mu / (\rho_0 - \rho))^{-1} = 2.5 \cdot 10^7$ $\text{s} \cdot \text{m}^{-2}$ (Figures 5.6i,j) and $g = 9.8$ $\text{m} \cdot \text{s}^{-2}$ this gives, in SI units:

$$t_D \sim 4.08 \cdot 10^{-6} \cdot k^{-1} \quad (5.21)$$

Similarly, the approximate magnitude of the residence time of fluid in the reaction zone (t_R) is given by:

$$t_R \sim \frac{L}{u} = \rho h \left[\frac{L^4}{g^2 F^2 \lambda (\Delta T)} \right]^{1/3} \cdot k^{-2/3} \quad (5.22)$$

For hot fluid at $\sim 400^\circ\text{C}$ the volumetric enthalpy is $\rho h \approx 10^9 \text{ J}\cdot\text{m}^{-3}$ (Figures 5.6e,f). With $L = 500 \text{ m}$, $g = 9.8 \text{ m}\cdot\text{s}^{-2}$, $F = 1.2 \cdot 10^{16} \text{ J}\cdot\text{s}\cdot\text{m}^{-5}$, $\lambda = 2 \text{ W}\cdot\text{m}^{-1}\cdot\text{K}^{-1}$, $\Delta T = 800 \text{ K}$, the reaction zone residence time, in SI units, is:

$$t_R \sim 1.395 \cdot k^{-2/3} \quad (5.23)$$

These residence time estimates are plotted as functions of permeability in Figure 5.8b. For the permeability assumed in Section 5.3 ($k = 10^{-14} \text{ m}^2$), the estimates deduced are $t_D \sim 4 \cdot 10^8 \text{ s}$ ($\approx 13 \text{ years}$) and $t_R \sim 3 \cdot 10^9 \text{ s}$ ($\approx 95 \text{ years}$). The estimate of 13 years residence time for the discharge zone is *much* larger than the estimate of a few minutes obtained by assuming that vent speeds are typical of the discharge zone (Section 5.1). (A discharge zone time of a few minutes would require an effective permeability as high as $4 \cdot 10^{-9} \text{ m}^2$, which would have to be provided by fault conduits.) It is important to note that the apparently large ascent time of $t_D \sim 13 \text{ years}$ is still sufficiently rapid for the fluid to suffer minimal conductive heat loss in the discharge zone and exit with the observed effluent temperatures (Figure 5.4). Elevated temperatures are maintained because the discharge zone has a relatively large half-width $L_D \sim 100 \text{ m}$ creating small horizontal temperature gradients and reducing conductive heat loss. The observation that of little conductive heat loss in the discharge zone confines its position somewhere between the following two extremes. At one extreme, the discharge zone may have large half-width (perhaps up to $\sim 100 \text{ m}$) for much of its height and a long residence time ($\sim 10 \text{ years}$). The observation that seafloor vents are so narrow ($\sim 0.1 \text{ m}$ to $\sim 1 \text{ m}$) suggests that the broad upflow in the discharge zone becomes focussed along fractures near the seafloor. At the other extreme the fractures which focus flow into vents may have deep penetration almost as far as the reaction zone. In the latter case, the discharge zone would have a half-width of the same order of magnitude as the vent diameter over most of its height. In turn, this would create very large horizontal temperature gradients and large conductive heat loss on ascent. This regime would demand correspondingly short residence times in the discharge zone to prevent significant cooling of the fluid on ascent.

The estimate derived for the reaction zone residence time ($t_R \sim 95 \text{ years}$ when $k = 10^{-14} \text{ m}^2$) is comparable on an order of magnitude scale with the radioisotope estimates (Kadko & Moore, 1988; Grasty *et al.*, 1988) of between 3 and 20 years. Assuming $L = 500 \text{ m}$, these residence times would be compatible with bulk permeabilities of $1.8 \cdot 10^{-12} \text{ m}^2$ and $1.04 \cdot 10^{-13} \text{ m}^2$ respectively and support the estimate of bulk permeability used in the model.

5.4.3 Axisymmetric scaling laws

In the previous section, scaling laws are derived for a two-dimensional plume in Cartesian geometry. It is also possible to consider the case of an axisymmetric plume rising above a magma chamber which is circular in plan form. In this case, Figure 5.1 should be interpreted as having an axis of rotational symmetry about the vertical centre line of the discharge zone. The velocity components (u, w) are now in the radial and vertical directions, but take the same form as before (equations (5.7) and (5.8)). However, the conservation of mass is now expressed by:

$$2\pi\rho uLH_R \sim \rho w\pi L_D^2 \quad (5.24)$$

From equations (5.7) and (5.8) for the velocities it follows that:

$$2H_R^2 \sim L_D^2 \quad (5.25)$$

Conservation of energy implies that:

$$\frac{\lambda\Delta T}{H_R}\pi L^2 \sim \rho hw\pi L_D^2 \quad (5.26)$$

from which it follows that:

$$\frac{L^2\lambda(\Delta T)}{L_D^2 H_R} \sim gkF \quad (5.27)$$

Equations (5.25) and (5.27) can be combined to give:

$$L_D \sim 2^{1/6} \left[\frac{\lambda(\Delta T)}{gF} \right]^{1/3} L^{2/3} k^{-1/3} \quad (5.28)$$

$$H_R \sim 2^{-1/3} \left[\frac{\lambda(\Delta T)}{gF} \right]^{1/3} L^{2/3} k^{-1/3} \quad (5.29)$$

Hence in the axisymmetric case, both the reaction zone thickness (H_R) and the discharge zone half-width (L_D) depend on permeability via the term $k^{-1/3}$. This is in contrast to the case of 2-d Cartesian geometry, where $H_R \sim k^{-1/3}$ (equation (5.14)), but $L_D \sim k^{2/3}$ (equation (5.13)). Thus, in axisymmetric geometry the reaction zone thickness and discharge zone half-width decay equally quickly as the permeability increases. However, in Cartesian geometry the discharge zone half-width decays faster than the reaction zone thickness. Since the velocities for the axisymmetric case take the same form as for Cartesian geometry (equations (5.7) and (5.8)) it follows that the residence times, t_D and t_R (equations (5.21) and (5.23)), apply equally to both geometries.

5.5 Conclusions

This chapter has been concerned with the control exerted by the nonlinear thermodynamic properties of water on hydrothermal convection cell structure. It has been shown that a very simple model of hydrothermal convection (Section 5.3) is sufficient to reproduce all of the expected features of a hydrothermal convection cell (Sections 5.1 and 5.2), providing the full nonlinear properties of water are retained. The model, which does not rely on inhomogeneous permeability or phase separation, is able to reproduce the thin reaction zone, narrow discharge zone, and temperature limited seafloor vents which are characteristic of all seafloor hydrothermal systems. This suggests that the dynamics associated with inhomogeneous permeability or phase separation are not required to explain convection cell structure, although both phenomena are important in active hydrothermal systems. By introducing a new concept, the ‘local Rayleigh number’ (Ra_L) it has been possible to predict how the nonlinear properties of pure water dictate the formation of plumes in a porous medium at $\sim 400^\circ\text{C}$, for seafloor pressures. The ‘fluxibility’ (F) of water has been shown to be of crucial importance to the formation of convective plumes in the seafloor. It has been argued that seafloor plumes form at the temperature (T_p) for which $|\partial F/\partial T|$ is maximised. For pure water at seafloor pressures, this plume formation temperature lies between 360°C and 440°C (Figure 5.7). The case of salt water convection is complex and requires thorough investigation. However, it is expected that a similar approach could be adopted.

The scaling analysis presented takes full account of the nonlinear thermodynamic properties of water. It has been shown how the lengthscales and residence times of the reaction zone and discharge zone depend on the permeability, on the assumption that this permeability is homogeneous. In principle, these scalings could be used to constrain bulk permeability if a robust estimate of the lengthscales or residence times could be made from active hydrothermal systems or fossil ophiolite systems.